JOURNAL OF Materials CHEMISTRY

Crystallization and textural porosity of synthetic clay minerals†

Kathleen A. Carrado,*[a] Roseann Csencsits,[b] P. Thiyagarajan,[c] Soenke Seifert,[a] Susan M. Macha[a] and John S. Harwood[d]

[a]*Chemistry Division, Argonne National Laboratory, 9700 S. Cass Ave., Argonne, IL 60439, USA. E-mail: kcarrado@anl.gov*
[b]*Materials Science Division, Argonne National Laboratory, 9700 S. Cass Ave., Argonne, IL 60439, USA*
[c]*Pulsed Neutron Source Division, Argonne National Laboratory, 9700 S. Cass Ave., Argonne, IL 60439, USA*
[d]*Department of Chemistry, University of Illinois at Chicago, 845 W. Taylor St., Chicago, IL 60607, USA*

Received 30th April 2002, Accepted 13th June 2002

The crystallization of synthetic layered magnesium silicate hectorite clays from both silica sol and organosilane sources is compared. For the silica sol-derived clays, a templating method is employed wherein organic or polymeric molecules are included during clay crystallization that are then removed from the composites *via* calcination. The mechanism of silane-derived hectorite formation is followed by XRD, TGA, ^{29}Si MAS NMR, and small angle X-ray scattering (SAXS), and results are compared to those obtained for the sol-derived hectorite. The mechanism appears to be similar but the rate is approximately doubled when the silane is used rather than silica sol. Analytical transmission electron microscopy (TEM) is exploited to glean structural morphology information towards resolving the nature of the resulting pore network structures. Results are compared with nitrogen adsorption–desorption isotherm behavior; dominant hysteresis loops are present in the type IV isotherms. Pore size distributions based on both the adsorption and desorption isotherms are compared. Small angle neutron scattering (SANS) experiments reveal that the average particle size increases as synthetic laponite < sol-derived hectorite < silane-derived hectorite < natural hectorite. Contrast matching SANS studies in aqueous and organic solvents are carried out to extract information about pore accessibility.

Introduction

Clays, which are layered silicate minerals, continue to evoke interest for basic research because of their applications to such diverse and technologically important fields as catalysis,[1] ion-exchange,[2] environmental issues,[3] and organic–inorganic nanocomposites.[4] This is especially true for the smectite class of clay minerals, wherein a so-called 2 : 1 primary unit consisting of two tetrahedral silicate layers that sandwich a central metal octahedral layer is separated from another *via* electrostatic interactions that arise from exchangeable cations in hydrated interlayers. Hectorite is the layered magnesium silicate variant of a smectite clay.[5]

A technique for making porous silicate heterogeneous catalysts from hectorite clay precursor sol–gels was developed recently in our labs.[6,7] A templating method is employed wherein organic or polymeric molecules are used during clay crystallization, which are subsequently removed *via* calcination. This results in a unique porous network, and these materials have proven to be adequate Co/Mo supports for hydrodesulfurization (HDS) catalysis.[8] Efforts to create and control the pore size or porosity characteristics of clays in general continue intensively, including pillared clay[9] and mesostructured clay systems.[6,7,10] The latter, mesostructured synthetic clays (MSCs), are based on hectorites that are crystallized from organo-containing silicate clay gels.[6] In this technique, *in situ* interlayer intercalation of different alkylammonium ions or polymers over broad molecular weight and concentration ranges is achieved. Upon removal of template by calcination the individual interlayer spaces collapse, but a stable and intact pore system remains from, presumably, the inter- and intra-tactoid volume. The use of polyvinylpyrrolidone (PVP) molecules or tetraethylammonium (TEA) cations yields materials with different porosity characteristics. Conversion of dibenzothiophene to biphenyl and biphenyl selectivities have been obtained from preliminary hydrodesulfurization tests, with encouraging results.[8]

For background information the reader is referred to an excellent review of the synthesis of smectite clay minerals in general, including hectorite clays.[11] The MSCs described above are crystallized from a gel that contains silica sol as the silicon source. A rigorous examination of the crystallization process of MSC hectorites was undertaken recently using ^{13}C MAS-NMR, ^{29}Si MAS-NMR, and small angle X-ray scattering (SAXS),[12] as well as XRD, TGA, and atomic force microscopy (AFM).[13] For comparison, a similar examination is reported here for a synthetic hectorite that is hydrothermally crystallized using an organosilane as the silicon source. The microstructure or extended network morphology of the MSC hectorites has not yet been identified, and it is believed that these characteristics would have the most effect on differences in catalytic behavior. Therefore, an in-depth analysis of nitrogen adsorption–desorption isotherm behavior, transmission electron microscopy (TEM) measurements, and contrast-matching small angle neutron scattering (SANS) results of the various synthetic hectorites is undertaken toward this goal.

Experimental

Materials

Since hectorite formation normally occurs under mild conditions, this has become our clay of choice for organic

---

†Basis of a presentation given at Materials Discussion No. 5, 22–25 September 2002, Madrid, Spain.

DOI: 10.1039/b204180b

incorporation.[14] The typical method for *in situ* hydrothermal crystallization of organo–hectorite clays is to create a 2 wt% gel of silica sol, magnesium hydroxide sol, lithium fluoride, and organic and to reflux in water for 2 days.[6,7] All chemical reagents, including a 30 wt% silica sol DuPont product (Ludox), were purchased from Aldrich. The PVP polyvinylpyrrolidone polymer molecular weights were 10 K, 29 K, 55 K, 360 K, and 1.3 M. TEA cations were obtained from tetraethylammonium chloride. Organic templates were removed by calcination at 500 °C for several hours. Precursor clay gel compositions are either: (a) 1.32 LiF, 5.3 $Mg(OH)_2$, 8 SiO_2, n H_2O, some with 10–30 wt% neutral PVP polymers added, or (b) 0.32 TEA, 1.0 LiF, 5.3 $Mg(OH)_2$, 8 SiO_2, n H_2O, to correlate with the ideal hectorite composition[5] of $Ex_{0.66}[Li_{0.66}Mg_{5.34}Si_8O_{20}(OH,F)_4]$, where Ex = exchangeable cation (Ex = Li or TEA). Note that Li(I) is an isomorphous substitution for Mg(II) at about 1 : 9.6. This gives rise to the net negative charge on the basal oxygen plane that is compensated for with the exchangeable Li or TEA cations. The silica sol-derived mixtures are refluxed for 48 h then centrifuged and the products are washed and air-dried. The products are referred to as Li-, TEA- or PVP-(silica)-hectorites before calcination, and as TEA- and PVP-MSCs after calcination.

For the silane-derived hectorite,[15] the molar ratios of Si : Mg : Li in the sol–gel were 0.5 : 1 : 0.25. A slurry of 1 wt% total solids in water is made using LiF, a freshly prepared $Mg(OH)_2$ sol,[6] and tetraethoxysilane (TEOS, $Si(OC_2H_5)_4$). All reagents were obtained from Aldrich. To make the clay, LiF is slurried in water for 30 min and the $Mg(OH)_2$ sol is added. This mixture is stirred for another 30 min, the silane is added, and heating is begun. It takes 30 min to reach reflux temperature. In one series of samples, the TEOS was diluted in water in a Teflon beaker and stirred for 30 min prior to addition to the sol; these are called "aged" silane samples. In another series of samples, the pH was raised slightly by washing the $Mg(OH)_2$ sol exhaustively (these sols do not settle and therefore a larger volume must be used). Normally the pH of the gel (or decant) after reaction ranges from 9.0–9.5, whereas the pH raises to 10 when the exhaustively-washed $Mg(OH)_2$ sol is used. The slurries were refluxed vigorously for various amounts of time then cooled, centrifuged, washed, and air-dried. This product is referred to as Li-(silane)-hectorite. TEA-(silane)-hectorite was made in a similar manner from a gel of composition 0.5 Si : 1.0 Mg : 0.125 Li : 0.125 TEA.

Comparisons were made to Laponite RD, a synthetic hectorite obtained from Southern Clay Products, Gonzales, TX, and SHCa-1, a California Na^+-hectorite from the CMS Source Clay Minerals Repository, Columbia, MO. SHCa-1 was first purified by sedimentation techniques to remove the 50% by weight $CaCO_3$ and iron impurities.

Characterization

XRD analyses were carried out on a Rigaku Miniflex+ instrument using Cu-K_α radiation, a fixed power source (30 kV, 15 mA), NaI detector, variable slits, 0.05° step size, and 0.50° 2θ min^{-1} scan rate. Powders were loosely packed in horizontally held trays. TGA-DTA (thermal gravimetric analysis and differential thermal analysis) measurements were obtained on a Seiko ExStar TG/DTA 6200 from Haake Instruments. The samples were measured against an alumina standard in a 100 ml min^{-1} O_2 flow with a temperature ramp of 10 °C min^{-1} to 800 °C. Some nitrogen adsorption and desorption isotherms were collected on a Quantachrome Autosorb-6 instrument. About 0.10 g of material was weighed into a Pyrex sample tube and evacuated to 80 mTorr overnight at room temperature, then backfilled with He. Most sorption data were obtained using a Micromiretics ASAP 2010. About 0.13 g of sample was degassed for 3 h at RT, 2 h at 110 °C, and backfilled with N_2. Pore size distributions were calculated using the Barett–Joyner–Halenda (BJH) method. Specimens for observation in the transmission electron microscope were prepared by placing 1 or 2 drops of clay suspension onto "holey" carbon films supported on copper grids. These specimens were allowed to air dry followed by a vacuum oven heating to 100 °C for 2 h. Specimens were imaged in a JEOL 100CXII transmission electron microscope operating at 100 kV. Bright field TEM images of clay particles are shown with selected area electron diffraction patterns included as insets.

The SAXS instrument was constructed at ANL and used on the Basic Energy Sciences Synchrotron Radiation Center undulator beamline ID-12 at the Advanced Photon Source.[16] The SAXS data were collected in just 0.02–0.20 s exposures (scans), even with the use of an aluminium foil absorber. Monochromatic X-rays at 10.0 keV were scattered off the sample and collected on a 9-element mosaic CCD detector (15 × 15 cm) run at 1536 × 1536 pixel resolution. The same powder samples as were used for all analysis methods (XRD, TGA, NMR, *etc.*) were sprinkled onto and sealed in scotch tape "cells". The scattered intensity has been corrected for absorption, scattering from blank scotch tape, and instrument background. The differential scattering cross section can be expressed as a function of the scattering vector Q, which is defined as: $Q = (4\pi/\lambda)\sin\theta$ where λ is the wavelength of the X-rays and θ is the scattering half angle. The value of Q is proportional to the inverse of the length scale (Å^{-1}). The instrument was operated at a sample-to-detector distance of 391 cm for the range $0.007 < Q < 0.16$ Å^{-1}. Error bars are not shown in any of the figures only for the sake of clarity; they are of equal or lesser size than the data points except at high-Q values.

^{29}Si NMR spectra were obtained using a Bruker DRX-500 NMR spectrometer equipped with a 4 mm CP-MAS probe. Samples were spun at speeds between 4.9 and 5.0 kHz. Bloch decay spectra were obtained using 256 scans, an approximate 90 degree RF pulse of 4 μ, a relaxation delay of 180 s, and an acquisition time of 43 ms. Proton decoupling was used during acquisition, employing a 64 kHz RF field strength and the two-pulse phase modulation scheme.[17] Samples were run at room temperature (*ca.* 295 K) without temperature control.

SANS measurements were performed using SAND, the time-of-flight SANS instrument at the Intense Pulsed Neutron Source at Argonne National Laboratory, using cylindrical Suprasil quartz sample cells with a path length of 1 mm. For these strongly scattering samples, SAND provides high-quality data in the scattering vector range of $0.0035 < Q < 0.8$ Å^{-1}. For the dry powder runs the cells were completely filled. For the contrast matching experiments the cells were 2/3-filled with the powder, solvent was carefully added to minimize swelling and to completely wet the samples, and the cells were capped. Based on the chemical composition and density, the calculated scattering length density of hectorite is 3.87×10^{10} cm^{-2}. Therefore, 64% D_2O/36% H_2O and 74% C_6D_6/26% C_6H_6 were used as contrast matching solvents. The scattering from an empty cell was used for background correction. Incoherent scattering cross-sections from the solvents determined from the high Q region of the data were used while fitting the low Q data to extract the power law exponents.

Results and discussion

Crystallization of Li-(silane)-hectorite

Previously, Carrado *et al.* exhaustively monitored the crystallization of TEA-(silica)-hectorite.[12,13] Consistent data from SAXS, XRD, TGA, atomic force microscopy (AFM), and IR using quenched aliquots *ex situ* were obtained. All of these techniques discerned clay crystallites beginning to form within the first few hours of reaction. ^{29}Si MAS NMR displayed a clay silicate peak after just 1 hour. Solid state ^{13}C NMR showed evidence of TEA-clay formation in as little as 30 minutes, and also revealed that 80% of the final TEA loading was accomplished in the first 10–12 hours. Up to 36 hours more is needed to incorporate the remaining 20% of TEA, indicating that a slower event dominates at the later stages of crystallization. A scenario was proposed where initial nucleation and crystallization end after about 14 hours, after which this occurs to a lesser extent and layer–layer stacking optimization and agglomeration of particles takes place. The SAXS data show this in progressively increasing power law values indicating more "open" structures that condense into more dense structures with time, and this correlates with observed AFM images.

XRD. Similar methods and techniques have now been applied to follow the crystallization of Li-(silane)-hectorite, where TEOS is used as the silica source rather than silica sol. Fig. 1 shows the XRD patterns for this clay as portions are quenched after various reaction times. At first, the primary peaks are due to the crystalline magnesium hydroxide (brucite) starting material. These peaks are assigned in Fig. 1. There is also a broad region near 22° 2θ that is assigned to amorphous silica. All of these features disappear at some point between 6 and 8 h. It is especially easy to gauge this by homing in on the peaks in the 55–65° 2θ range where two brucite peaks disappear and one clay peak grows in. In addition, the clay (110) and brucite (001) peaks are close together (at about 19° 2θ) and overlap to some extent, but they are distinctly separate. Hectorite clay peaks, which are also assigned in Fig. 1, are visible as early as 4 h. When samples are crystallized with a gel molar composition of Si = 0.4 rather than 0.5, the *d*(001) peak (the crystallographic unit cell dimension along the *c*-axis which includes both the clay 2 : 1 lattice and one interlayer) is never as intense or sharp as the Si = 0.5 sample, and the disappearance of brucite and silica peaks does not occur until sometime between 10 and 17 h of reaction (figure not shown). Therefore, the Si = 0.4 clay takes twice as long to crystallize and does not orient as well as the Si = 0.5 sample. Li-(silane)-hectorite (at Si = 0.5) where the TEOS silica source is "aged" prior to use by diluting in water and pre-mixing for 30 min gives very similar XRD results as when the silane is used fresh (figure not shown). Therefore "aging" (as is done for some mesoporous silica formulations) is not necessary for this clay synthesis. One additional point is brought out by the comparisons made in Fig. 2 for various 6 h samples. Note that the brucite appears to be used up more quickly when an aged TEOS solution is employed, and more quickly still when the gel pH is raised from 9.5 to 10. However, in both cases the *d*-spacing loses definition and in the latter case it is extremely broad.

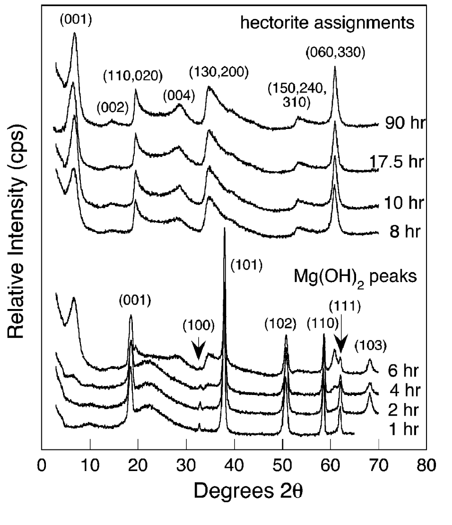

Fig. 1 XRD patterns of Li-(silane)-hectorite aliquots that are quenched at various reaction times (unaged silane); reaction times and assignments are indicated on the plot. Gel molar composition of Si = 0.5, Mg = 1, Li = 0.25.

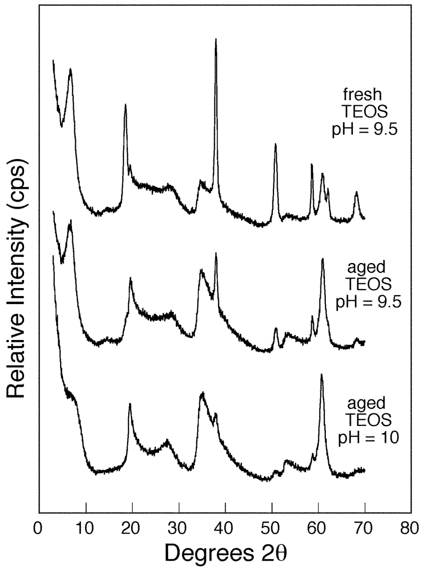

Fig. 2 XRD patterns of Li-(silane)-hectorite aliquots quenched at 6 h under various conditions as indicated on the plot.

Thermal analysis. Fig. 3 shows TG/DTG plots for some of the Li-(silane)-hectorite aliquots that were shown in Fig. 1. Magnesium hydroxide dehydroxylation/dehydration takes place as a clearly visible sharp event at 370 °C, with the amount of weight lost decreasing from 10.6, 7.2, and 5.4 wt% for the 2, 4, and 6 h samples, respectively. As was observed in the XRD results, none of this phase is apparent in the 8 h sample and beyond. In these fully crystallized latter samples, only interlayer dehydration and clay lattice dehydroxylation are observed at about 50 °C and 725 °C, respectively. Similar TG/DTG results are observed for the Li-(silane)-hectorite

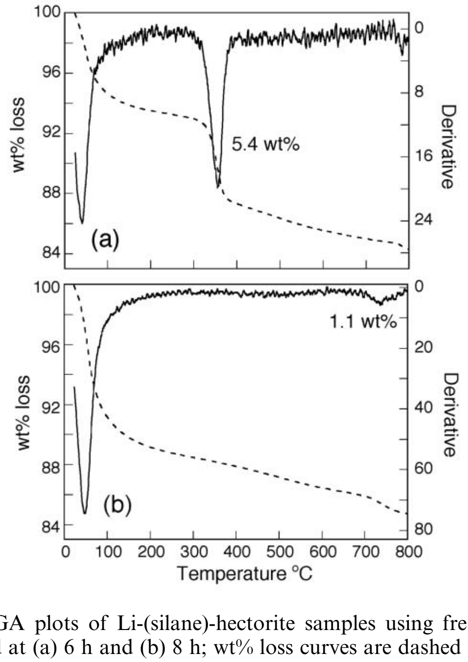

Fig. 3 TGA plots of Li-(silane)-hectorite samples using fresh TEOS quenched at (a) 6 h and (b) 8 h; wt% loss curves are dashed (left axis) and first derivative DTG curves are solid (right axis).

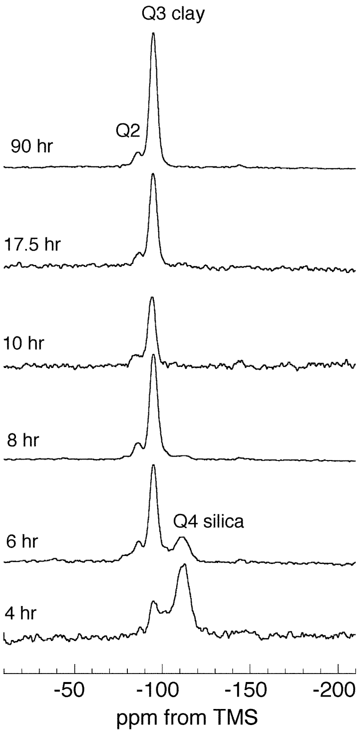

Fig. 4 ^{29}Si MAS NMR results for the Li-(silane)-hectorite aliquots using fresh TEOS.

aliquots made using the "aged" TEOS silica source (results not shown), although for some reason in this case the $Mg(OH)_2$ dehydroxylation peak steadily decreases from 375 °C to 346 °C going from the 2 h to the 6 h sample.

^{29}Si MAS NMR. Fig. 4 displays the ^{29}Si MAS NMR results for the Li-(silane)-hectorite aliquots. The peak at -95 ppm is assigned to the tetrahedral $Q3$(0Al) $Si^*(OMg)(OSi)_3$ site reported previously for this clay.[15] It also appears at -94 to -95 ppm for natural hectorites,[18] at -94 ppm for synthetic hectorite made using silica sol (TEA-(silica)-hectorite),[12] and at -94.4 ppm for the synthetic hectorite called laponite.[19] The term $Q3$ refers to the number of branching units typical of sheet silicate structures, and (0Al) indicates that no aluminium is present to affect the chemical shift (the presence of aluminium is ubiquitous in most natural sheet silicates). The higher field peak for the $Q4$ tetrafunctional $Si(OSi)_4$ units typical of silica is observed only at early reaction times, and its intensity decreases with reaction time. This peak also occurs at -112 ppm for TEA-(silica)-hectorite[15] and for the colloidal silica sol Ludox HS-40 the $Q4$ peak has been reported at -107 ppm.[20] There is an additional small contribution at -85 ppm to -87 ppm that appears at 4 h of reaction time and persists throughout crystallization. The chemical shift for a $Si^*(OSi)_2(OH)_2$ species has been reported at -89 ppm.[21] A peak at -85 ppm has been observed in silica sols as the particle size decreases and assigned to a $Q2$ branching species that contains two hydroxyl groups.[20] This peak is therefore assigned to either an incompletely condensed $Si^*(OMg)(OSi)_2(OH)$ unit or to a $Si^*(OSi)_2(OH)_2$ species. Synthetic hectorites made from silica sol also show evidence of this feature, especially at intermediate crystallization times.[12]

SAXS data. Fig. 5 displays the SAXS data for Li-(silane)-hectorite powder aliquots, derived using fresh TEOS, for 2–8 h of crystallization time. The curves after 8 h are very similar and so are not shown for the sake of clarity. Dramatic differences in the SAXS data appear between 4 and 6 h when the peak at about $Q = 0.03$ Å^{-1} disappears, in contrast to the other techniques that showed more differences between 6 and 8 h. Very similar plots were obtained for the Li-(silane)-hectorites derived from aged TEOS (not shown). All of the curve shapes for the Li-(silane)-hectorite samples beyond 6 h of reaction time are similar to each other and, more interestingly, their features are collectively quite different from the SAXS curves obtained for TEA-(silica)-hectorite.[12]

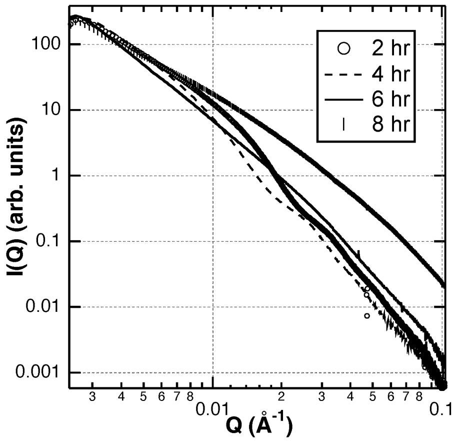

Fig. 5 SAXS of Li-(silane)-hectorite powder aliquots, using fresh TEOS, quenched at early crystallization times (2–8 h). Curves beyond 8 h were very similar and so are not shown for the sake of clarity. Error bars are also not shown for clarity (they are of smaller or comparable size to the data points).

From all of the preceding data, a general view has emerged regarding the crystallization of Li-(silane)-hectorite. It appears to be similar to that of TEA-(silica)-hectorite, wherein initial clay nucleation begins with hydroxylated silica species condensing onto the pre-existing brucite sheets. At the same time, and during the LiF/brucite stirring period prior to silane addition, lithium(I) and magnesium(II) undergo isomorphous substitution. For TEA-(silica)-hectorite this crystallization period takes 12–14 hours under these particular hydrothermal conditions. The data here show that this period is substantially decreased for Li-(silane)-hectorites, down to 6–8 hours. Presumably this is because the silica sol needs time to dissolve and form the silicate precursor species that are in contrast immediately available when the TEOS silane is used. After the initial crystallization is complete in either case, layer–layer stacking optimization and agglomeration of particles takes place. All of the data show that essentially the clay is formed and starting materials are used up by 8 h using the hydrothermal conditions employed here. Slight modifications of certain synthetic variables greatly effect the extent of clay crystallization at earlier times, however. The effect of pH and silane "aging" were shown, and the importance of stirring LiF and brucite together for 30 min prior to silane addition was mentioned. The quality of XRD patterns is highly dependent upon these variables at times less than 8 h. Even after the aliquots are quenched and the powders collected, the XRD quality for these intermediate samples changes with time (data not shown). Specifically, the relative amounts of brucite and clay, at least in terms of XRD peak intensities, are observed to change over the timespan of a few months.

Comparison of physical properties, including textural porosity

Elemental analysis results of Li-(silane)-, Li-(silica)- and TEA-(silica)-hectorites are shown in Table 1. The Li-(silica)-hectorite was not characterized much beyond this point because of its very low reactivity in HDS tests; TEA-(silica)-hectorite, on the other hand, was very active.[8] In the ideal hectorite composition, the Si/Mg molar ratio is 1.5. Experimentally it is very close to that of the Li-(silane)-hectorite at 1.4. The ratio is near 2, however, for the silica-derived clays. This calculates to an

Table 1 Elemental analysis results for various synthetic hectorites

Clay	wt% Si	wt% Mg	wt% Li	Si/Mg[a]
Li-(silane)	23.4	14.6	0.86	1.4
Li-(silica)	26.6	11.9	0.74	1.9
TEA-(silica)	27.3	11.0	0.35	2.1

[a] Molar ratio, ideal hectorite Si/Mg = 1.5.

excess of about 3.5 moles of silica per mole of clay, or about 20 wt% impurity. This excess silica has been observed by a variety of techniques, most notably *via* ^{29}Si MAS-NMR,[12] and it has proven difficult to reduce and/or remove.

The XRD patterns of synthetic Li- and TEA-hectorites derived from both silica sol and silane sources are shown in Fig. 6. In these patterns all of the expected peaks for hectorite are present and at the same time there are no peaks due to starting materials. Peak assignments for hectorite are indicated directly on Fig. 6a. The *d*-spacing along the *c*-axis (*d*(001)) ranges from 12.8–13.3 Å for the Li-clays to 14.7–14.8 Å for the TEA-clays. Regarding the latter, the larger value simply corresponds to the larger size of the TEA cation. There are other similarities that arise when the cation changes from Li to TEA. Specifically, note the pattern of higher order (00l) reflections. For Li-clays the (002) and (004) reflections are readily apparent whereas for the TEA-clays, it is the (004) and (005) reflections which appear.

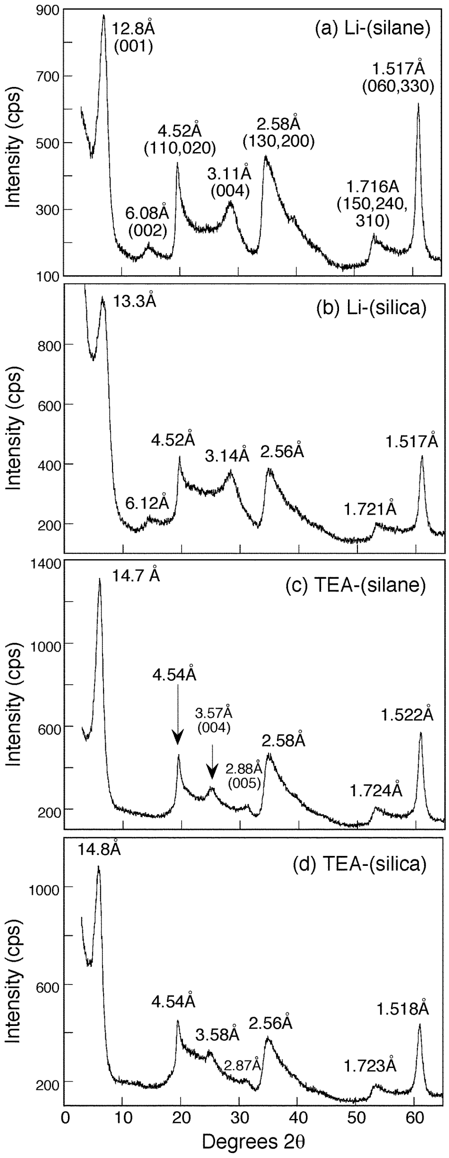

Fig. 6 XRD patterns of synthetic Li- and TEA-hectorites derived from both silica sol and silane sources as indicated directly on the plots.

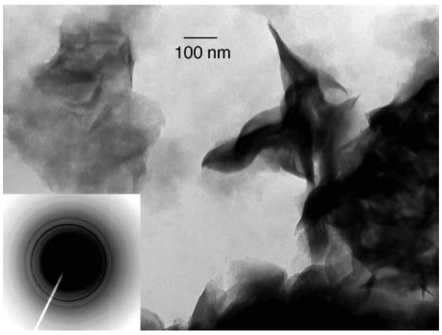

Fig. 7 TEM of Li-(silane)-hectorite with scale bar and electron diffraction pattern inset.

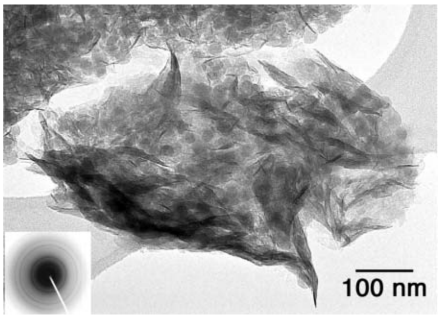

Fig. 8 TEM of TEA-(silica)-hectorite with scale bar and electron diffraction pattern inset.

TEM. Fig. 7 and 8 show the TEM images of Li-(silane)-hectorite and TEA-(silica)-hectorite, respectively. The electron diffraction patterns clearly show the presence of hectorite in both cases. Two structural morphologies are present in the silica-derived sample: a 15–30 nm sphere- or disk-like phase and one that is more traditionally consistent with the smectite morphology of long, thin flexible plates. Since it is known that there is excess silica sol in these clays, the smaller phase is most likely due to spheres of the starting material silica sol. Note however the large amount of thin "lines" of about this same length scale, which would be expected if small clay disks were viewed edge-on. This could also happen if small single clay plates curled up at the edges, and there is some indication of this in Fig. 8. The Li-(silane)-hectorite in Fig. 7 also shows some of this behavior, albeit on a longer length scale (50–100 nm). Note also the complete lack of smaller disks or spheres. Fig. 9 is the TEM of the pure silica sol and it shows very uniform and regular particles of the order of 20–25 nm, without any indication of the 25–50 nm thin "plates" present in TEA-(silica)-hectorite. The conclusion is that the silica-derived

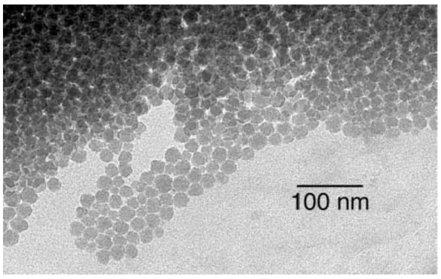

Fig. 9 TEM of the silica sol used in (silica)-hectorite preparations.

samples have a fairly wide range of clay particle sizes along with the presence of some silica sol, while the silane-derived clays display larger, more uniform particle sizes which are on the whole more typical of natural hectorites.

TEM analysis of the mesostructured synthetic clay (MSC) systems was then undertaken. Recall that these clays are crystallized in the presence of an organic or polymeric template that is removed upon calcination, leaving presumably some type of porous imprint behind. No significant differences for the calcined TEA-MSC were discernible when compared with the TEA-(silica)-hectorite TEM of Fig. 8 (data not shown). This is not surprising since it is assumed that in this case the TEA cations are located within the gallery regions, and their removal would not affect the overall mesostructure or morphology of the clay. Fig. 10 shows the TEM images of two synthetic polymer–hectorites derived using silica sol as the silicon source (where PVP is the polymer). Fig. 10a is a fresh, uncalcined PVP-(silica)-hectorite, while Fig. 10b is a calcined PVP-MSC. The images are very similar to the TEA-(silica)-hectorite samples (Fig. 8) in that they show no readily discernible changes resulting from calcination. Since the polymer is loaded at only the 10 wt% level for these samples, it is not surprising that the results are similar to the TEA system upon calcination. Therefore, on the whole, all of the silica-derived hectorites are similar to each other and, at the same time, quite different in morphology from the silane-derived clays (see Fig. 7). The silica-derived clay images show micron-sized particles with highly "textured" or rough surfaces with many flexible clay plates oriented outwards in multiple directions on a small length scale ($\approx$100 nm), which does not occur with the larger silane-derived clay plates. These scaly crackled surfaces give rise to an overall open morphology on a certain length scale. It is speculated that these features may result because of the silica sol spheres, which may act to physically keep small stacks of clay sheets apart, as well as fostering a smaller particle size. (Note that there is no evidence of silica sol pillaring, which would have appeared in the SAXS curves.[12])

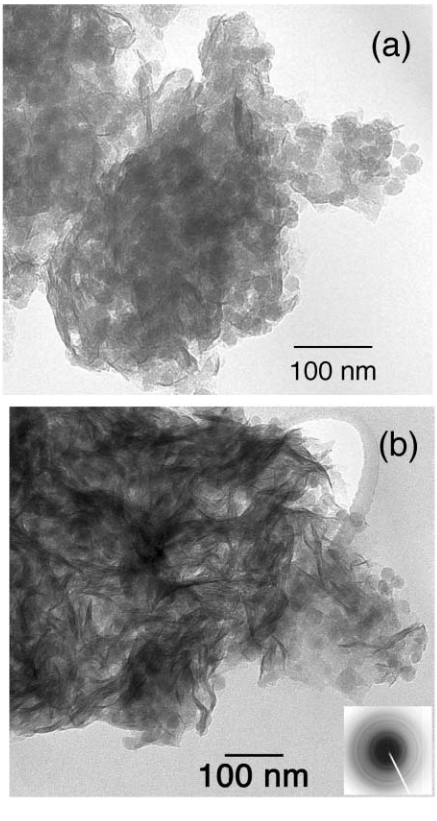

Fig. 10 TEM images of (a) a synthetic (silica)-hectorite containing 10 wt% PVP polymer (M_W = 55 K) and (b) a calcined synthetic (silica)-hectorite that had 10 wt% PVP polymer (M_W = 360 K); electron diffraction pattern inset indicates clay.

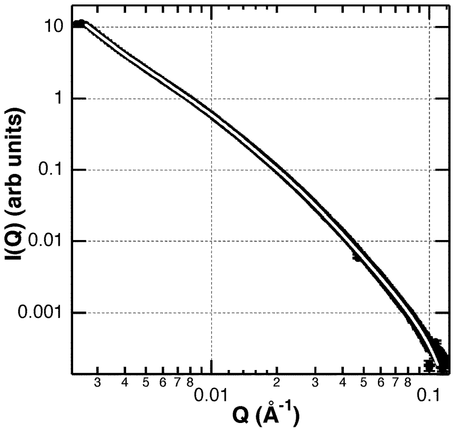

Fig. 11 SAXS of Li-(silane)-hectorite (90 h sample with fresh TEOS) fitted over the entire range with the unified exponential/power law equation[22] (white line) using 2 layers. The reduced χ^2 for this fit was 7.8.

Differences in surface textural properties are also borne out in the SAXS data. Curves for silica-hectorites are modeled best as "fractal aggregates of lamellae",[12] whereas the silane-hectorites do not model well to this equation. The silane-hectorites instead model better to the generic unified exponential/power law approach developed by Beaucage,[22] from which the specific fractal aggregates of lamellae equation is derived, without any specific parameters for lamellar disks. Fig. 11 shows one representative fit as an example (the 48 h sample data is very similar to the 90 h sample, especially at mid- and high-Q values). This approach has been demonstrated to work exceedingly well for scattering from complex systems that contain multiple levels of related structural features, including polymer blends, silicas, and activated carbons.[23] In this approach, one structural level includes both a Guinier regime and it's corresponding power law regime. The fits here model best with two structural levels, each with their own resultant radius of gyration values (Rg) for the Guinier regime and power law exponents. For the first structural layer, the Rg was set arbitrarily to a very large value (1000 Å) to derive the power law exponent, which is 2.17; for the second structural layer, Rg = 143 Å ($\pm$ 0.4 Å) and the power law exponent is 3.32.

Sorption data. Fig. 12 shows the adsorption–desorption N_2 isotherms for representative hectorite clays. These include mesostructured synthetic clays (MSC), where the initial organic template present (be it polymer or TEA) is removed *via* calcination. PVP-(silica)-MSCs, can be divided in behavior into those made using lower molecular weight (10–55 K) and larger molecular weight polymer (360 K–1.3 M). All of the isotherms are closest in shape to type IV because hysteresis in the multilayer range of physisorption isotherms occurs, which is often associated with capillary condensation in mesopore structures.[24] There are clear differences in the shapes of their hysteresis loops, however. Laponite, TEA-(silica)-hectorites, Li-(silane)-hectorite, and PVP-MSC samples made using lower molecular weight polymers display type H2 hysteresis behavior, while SHCa and the higher molecular weight PVP-MSC samples display type H3 loops.[24] Type IV adsorption isotherms usually flatten at high P/P_0, but a final upward turn is often observed. This is due to capillary condensation in macropores or in interstices between grains.[24] In terms of just the adsorption isotherms (which is most often reported for clays, see *e.g.* ref. 25), laponite's curve is unique from all the rest. It

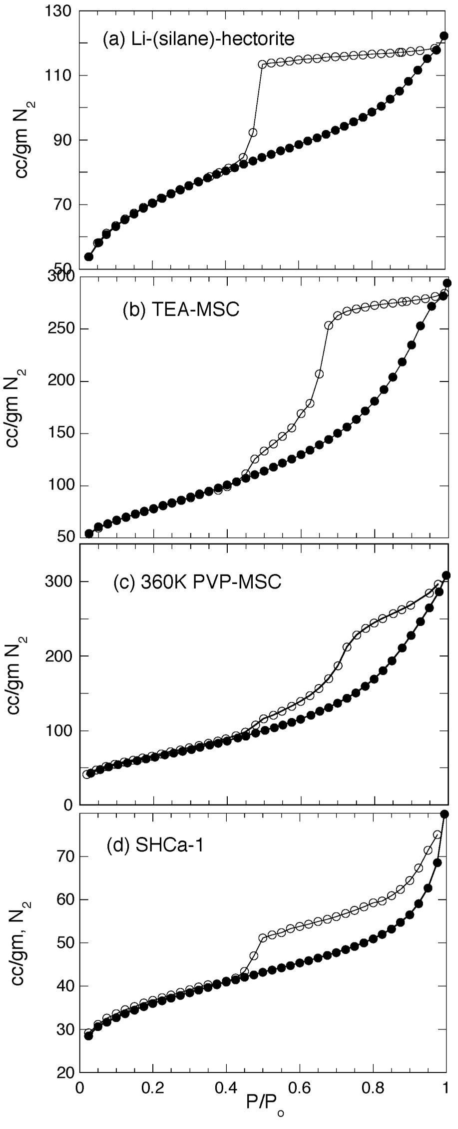

Fig. 12 Nitrogen sorption isotherms (type IV) with H2 hysteresis loops for (a) Li-(silane)-hectorite, (b) calcined TEA-(silica)-hectorite (TEA-MSC) and H3 hysteresis loops for (c) 360 K PVP-MSC and (d) purified natural hectorite SHCa; filled circles adsorption, open circles desorption.

does not exhibit a "knee" (commonly called point B[24]) at low P/P_0 values, the beginning of a near linear middle section of the curve, which indicates the point where monolayer coverage is complete and multilayer adsorption begins.

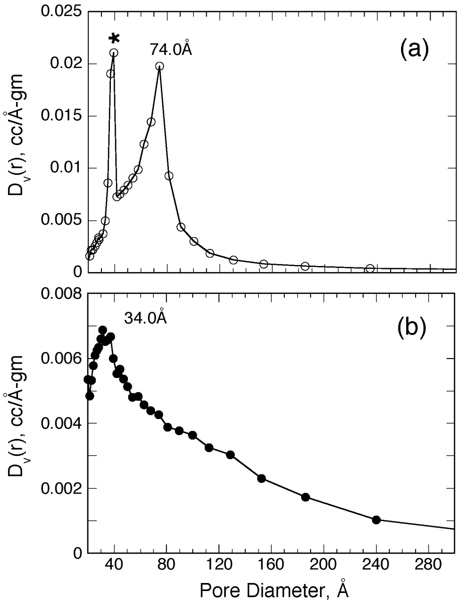

Fig. 13 Pore size distributions based on (a) desorption and (b) adsorption isotherms for 360 K PVP-MSC (calcined synthetic 360 K PVP-(silica)-hectorite); * = nitrogen sorbent "knee" artifact for layered materials.

Generally the specific surface areas and pore size distributions (PSDs) from type IV isotherms are quite reliable; for those with type H2 hysteresis loops the adsorption branch is best used.[24] Because the particular adsorption isotherms shown here are very broad, the corresponding PSDs based on adsorption branches are also rather broad. Regarding the desorption isotherm branches, the type H2 hysteresis loops, while common, are difficult to interpret and are vaguely attributed to mesoporous networks of "broad" structure.[24] The desorption branch can be more reliably used for pore size determinations with type H3 hysteresis. Type H3 loops are observed for aggregates of plate-like particles giving rise to slit-shaped pores.[24] Fig. 13 displays the adsorption and desorption pore size distributions (BJH method) for 360 K PVP-MSC, a clay that displays type H3 hysteresis, as representative behavior. Table 2 summarizes surface area and porosity results for all of the clays examined. (Note that pure SHCa is microporous and therefore not amenable to the BET equation, which is true when high or negative *C* values are obtained.[26]) In Table 2 it is the average values from several different syntheses that are reported. The largest variability occurs in the pore diameters calculated from the desorption curves. Recall that, even though BJH(des) values are reported in Table 2, they are

Table 2 Surface areas, pore volumes, and pore diamaters of various hectorites from N_2 porosimetry measurements (averages from several trials)

Clay	BET S.A./m^2 g^{-1}	*C* value[a]	P.V.[b]/cc g^{-1}	avg. BJH(ads) P.D./Å	avg. BJH(des) P.D.[c]/Å
laponite	378	325	0.26	43	
laponite, calc.	267	80	0.25	44	
Li-(silane)	252	368	0.14	47	
Li-(silane), calc.	186	333	0.13	51	
Li-(silica)	265	114	0.34	52	
Li-MSC[d]	237	155	0.32	53	
TEA-(silica)	363	160	0.39	56	46
TEA-MSC	332	138	0.57	69	54
55 K PVP-(silica)	369	163	0.48	55	44
55 K PVP-MSC	260	90	0.40	56	44
360 K PVP-(silica)	259	156	0.39	65	57
360 K PVP-MSC	270	103	0.50	68	66

[a] This BET constant should be within 50 and 300; if >300 then S.A. should be <500 m^2 gm^{-1} to be reliable;[26] correlation coefficients are $\geqslant 0.9999$. [b] Average of BJH adsorption and desorption pore volumes; in all cases the micropore volume is $\leqslant 0.04$ cc gm^{-1}. [c] The peak observed at 38–40 Å was ignored; all samples had this peak and, in the cases where no value is reported, it was the only peak. [d] MSC = mesostructured synthetic clay formed *via* calcination of corresponding (silica)-hectorites.

not reliable values in most cases and are reported for the sake of very general comparisons only. Even the 360 K PVP-MSC, which has the more reliable H3 loop, has a PSD(des) peak that is quite sharp but varies batch-to-batch from 54 Å to 77 Å; for TEA-MSCs it varies from 51 Å up to 110 Å. The clay with the highest hydrodesulfurization activity was TEA-MSC,[8] which is not surprising since it is also the clay in Table 2 with among the highest surface area, highest pore volume, and largest adsorption pore diameter values.

One last feature to notice is that in all of the isotherms the desorption branch shows an inflection "knee" at about 0.45–0.5 P/P_0. This gives rise to a sharp peak at 37–39 Å in the desorption PSD that has been observed for many different types of layered materials when using nitrogen as the sorbent gas (nitrogen boils at $P/P_0 \approx 0.42$), and it is therefore ignored. The phenomenon arises due to the complexity of capillary condensation in pore networks with pore blocking effects.[24]

SANS data. Small angle neutron scattering (SANS) is a versatile technique for the characterization of porous solid materials with high sensitivity on length scales of 1–100 nm. Because SANS arises from inhomogeneities in the neutron scattering length density of a particular system, the scattering data can provide information about the size, morphology, and organization of pores in solids as well as their accessibility to solvents. For a better understanding of the nano- and mesoscopic network structures present in the synthetic clays, a contrast matching SANS study was performed using aqueous and organic solvents with neutron scattering length densities designed to mask the scattering from the clays. It is hoped that the scattering signal from the contrast matching studies will highlight the presence of inaccessible pores and/or particles having chemical compositions that differ from hectorite.

Morphological information can be obtained by using the modified Guinier analysis for sheetlike objects, a plot of $Q^2I(Q)$ *vs.* Q^2, which is shown in Fig. 14 for several hectorites. The presence of a linear region in such a plot at low Q indicates that the particles are lamellar. The slope of the linear region at $QR_t \leqslant 1.0$ is R_t^2, where R_t is the average thickness factor of the sheet. From this the average thickness of a clay tactoid (assemblage of stacked clay lamellae in the powder) can be determined as slope$^{1/2}(12^{1/2})$ (or $R_t \times \sqrt{12}$). A notable feature in the modified Guinier plots for the clays is that, depending on the clay, the linear correlation breaks down at certain Q^2 values and the curve begins to fall off below these values. The bend over of the curve indicates that the lamellar particles have a finite lateral size, and the Q value corresponding to the bend over region gives a qualitative idea of the lamellar lateral extent. Table 3 lists the thicknesses and the approximate Q values corresponding to the bend over regions for several synthetic hectorites, including laponite, and a natural hectorite. Interestingly, several of the clays exhibit two linear and corresponding bend over regions (see *e.g.* Fig. 14b), implying two distinct populations of lamella with different thickness and lateral extension. Both the thicknesses and aspect ratios (a measure of width/height) therefore increase as: laponite < PVP-MSC < TEA-MSC < Li-(silane)-hectorite < natural hectorite.

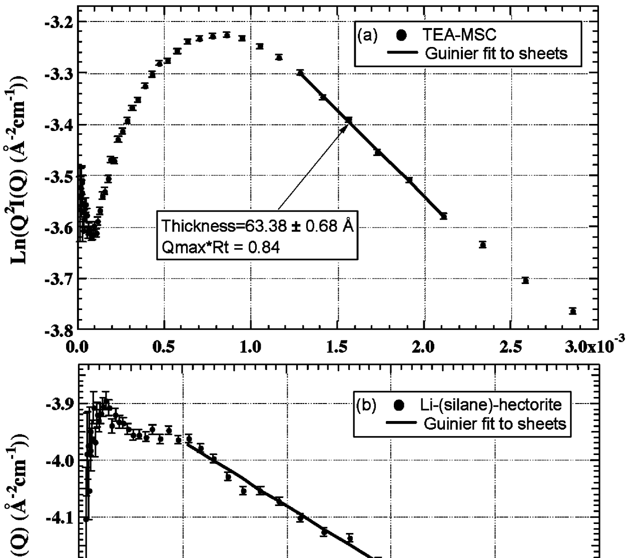

Fig. 14 Modified Guinier analysis of SANS data from powders of: (a) calcined TEA-(silica)-hectorite (TEA-MSC) and (b) Li-(silane)-hectorite. Note the differences in the Q^2 ranges to fulfill the Guinier approximation.

Table 3 Data from modified Guinier sheet analysis of SANS data (Fig. 14) for various hectorite powders

Clay	Tactoid thickness/Å	No. of layers per tactoid[a]	Bend over point, Q^b/Å^{-1}
laponite	20.1	2	0.045
360 K PVP-MSC	36.7	4	0.063
	75.4	7	0.035
1.3 M PVP-MSC	36.3	4	0.063
	83.1	8	0.035
TEA-MSC	63.4	6	0.028
Li-(silane)-hectorite	79.0	6	0.014
	102	8	0.0071
SHCa	large[c]	large[c]	none[c]

[a] One clay platelet is approx. 9.6 Å; one clay layer including interlayer gallery region (d(001)) is approx. 10 Å for calcined clays (MSCs) and approx. 12–15 Å depending upon the exchangeable cation size for unheated clays. [b] Note that values are in Q, not Q^2 as presented in Fig. 14; entries are generally arranged with decreasing Q values which indicates increasing lateral size. [c] No linear slope due to a large amount of stacking and polydispersity in the thickness; the lateral extent may be in the micron range, therefore there is no bend over in this Q region.

One of the advantages of SANS is the ability to tune the contrast between a sample and its environment, or different parts of a sample, by varying the isotopic substitution of hydrogen with deuterium due to the large difference between their scattering lengths. Water was chosen because it is known to wet clays well and is expected to access all open networks available. Other groups have used D_2O as well as C_6D_6 to study the pore and pillar distributions in pillared clays.[27] The magnitude of the power-law exponents in the low Q region of the scattering data provides information on the morphology of the particles, such that the scattering signal for an infinitely thin rod with length L varies as[28] Q^{-1} at $QL >> 1$ and for a thin flat plate with lateral dimension R it varies as[29] Q^{-2} at $QR >> 1$. In the case of fractal objects the power-law scattering extends to wide Q ranges with power-law exponents in the range[30] of 1 to 3, depending on the density of the system. Surface fractal objects have power-law exponents in the range[31] of 3 to 4. According to Porod,[32] particles with a smooth boundary will have a power-law exponent of 4. Higher power-law exponents have been observed in the scattering data for certain porous silicas; Schmidt and co-workers[33] successfully interpreted this to be due to a "fuzzy" pore boundary where the density varied smoothly rather than discontinuously as in the case of smooth objects.

Table 4 lists the magnitude of the power-law exponents derived for the clays in their dry state as well as when they are imbibed in the contrast matching water and benzene solvents.

Table 4 Power law exponents[a] from SANS contrast variation studies

Hectorite	Powder	64% D_2O/ 36% H_2O	74% C_6D_6/ 26% C_6H_6
SHCa	4.58	C.M.[b]	3.21
laponite	3.40	C.M.	2.90
Li-(silane)	1.96	4.13	2.23
TEA-MSC	2.13	2.21	2.37
360 K PVP-MSC	2.42	2.83	2.46
1.3 M PVP-MSC	2.23	3.09	2.41

[a] In $0.004 < Q < 0.009$ Å^{-1} range; reduced χ^2 values were all $\leqslant 2.27$ (most were $\leqslant 1.3$). [b] C.M. = contrast matched, no coherent scattering signal.

The power-law exponent for SHCa is 4.58 which falls into the category of a porous solid with fuzzy pore boundaries. This means that the particle surface near the pore boundary may have large density variation when compared to its interior. In contrast, laponite powder exhibits a power-law of 3.4 which resembles a surface fractal. Interestingly the coherent scattering from these two clays is completely suppressed when exposed to 64% D_2O/36% H_2O, implying that the entire pore network is accessible to water. However, a significant amount of coherent scattering persists when they are in the contrast matching benzene solvent, with power-law exponents of 3.21 and 2.9 for the SHCa and laponite, respectively. This scattering signal therefore may be due to a portion of the pore network that is inaccessible to benzene, due to either size or hydrophobicity effects.

In the case of synthetic clays we observe quite different scattering behavior with power-law exponents for the dry powders in the region of 2 (see Table 4). This along with the results from Table 3 implies that these synthetic clays are smaller and better dispersed than the natural clay. The slightly larger power-law exponents for the clays synthesized in the presence of polymers may be due to their higher density caused by the presence of a larger volume fraction of tactoids. Fig. 15 shows representative scattering data for the TEA-MSC and Li-(silane)-hectorite under different conditions. The scattering curves differ in shape for these two different synthetic clays due to the difference in their nano- and micro-structure, as well as their accessibility to aqueous and organic solvents. The scattering intensities for the clays do decrease substantially in the contrast matching solvents. Interestingly, unlike either SHCa or laponite, these clays cannot be contrast matched completely using either water or benzene, as evidenced by the large power-law exponents in their scattering signals. This means that in these clays a significant portion of pore network is inaccessible to either water or benzene. Although the accessibility of benzene seems to be similar in all synthetic clays based on the similar power-law exponents in Table 4, the accessibility of water in the network displays more variability. More in depth analysis of the scattering curves (both neutron and X-ray) will be published at a later date.

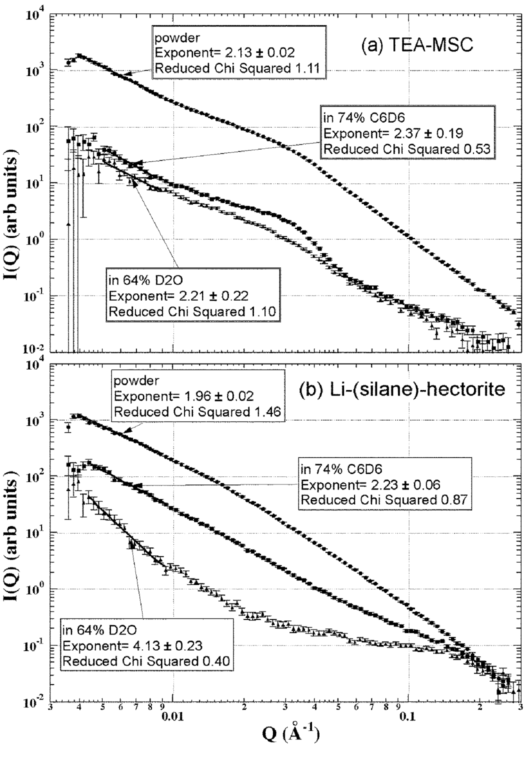

Fig. 15 SANS of two synthetic clay systems (a) TEA-MSC and (b) Li-(silane)-hectorite in powder form, and in 74% C_6D_6/26% C_6H_6 and 64% D_2O/36% H_2O contrast matching solvents with power law fits indicated at low Q.

Conclusions

A general view has emerged regarding the crystallization of hectorite. Initial clay nucleation begins with hydroxylated silica species condensing onto the pre-existing brucite sheets. At the same time, and during the LiF/brucite stirring period prior to silane addition, lithium(I) and magnesium(II) undergo isomorphous substitution. For TEA-(silica)-hectorite this crystallization period takes 12–14 hours under these particular hydrothermal conditions. This time is substantially decreased for Li-(silane)-hectorites to 6–8 hours. Presumably this is because the silica sol needs time to dissolve and form the silicate precursor species that are immediately available when a silane is used. "Aging" of the silane by previous stirring in water does not enhance crystallization, however. Rather, the time does not decrease and in addition the quality of the *d*-spacing (a measure of layer–layer optimization) decreases. No matter which silicon source is employed, after the bulk of the crystallization is complete, layer–layer stacking optimization and agglomeration of particles takes place. Preliminary results show that this synthesis is also amenable to use of an autoclave. For example, a Li-(silane)-hectorite with only a trace amount of brucite before washing was crystallized in 6 h at 200 °C under autogenous pressure.[34]

In terms of textural porosity, the silica-derived clay images show micron-sized particles with highly "textured" or rough surfaces with many flexible clay plates oriented outwards in multiple directions on a small length scale (≈ 100 nm). These scaly crackled surfaces give rise to an overall open morphology on a certain length scale. It is speculated that these features may result because of the silica sol impurity, which may act to physically keep small stacks of clay sheets apart, as well as fostering a smaller particle size. This does not occur with the larger silane-derived clay plates which instead display a morphology much more typical of smectite clays. Both the thickness of clay tactoids and their aspect ratios are found to increase in SANS experiments as laponite < PVP-MSC < TEA-MSC < Li-(silane)-hectorite < natural hectorite. TEM measurements also bear this out. The synthetic sol- and silane-derived clays are smaller and better dispersed than the natural clay as revealed by SANS.

Acknowledgements

The input of R. Kizilel (Ill. Inst. Tech.), R. E. Winans and G. Sandi-Tapia (both CHM ANL) regarding SAXS analysis and the assistance of D. Wozniak (PNS ANL) with SANS measurements is greatly appreciated. A. Essling and S. Lopykinski performed the %Si, Mg, Li analysis using ICP-AES (Analytical Chemistry Lab, ANL). J. Gregar (CHM ANL) fabricated some of the nitrogen porosimetry and SANS cells. We would like to acknowledge the National Science

Foundation for their funding of the solid-state NMR equipment used in this work (grant CHE-9974802). This research was performed under the auspices of the U.S. DOE-BES, Division of Chemical Sciences, Geosciences, and Biosciences (K. A. C., S. S., S. M. M., contract #W-31-109-ENG-38) and Materials Sciences (P. T., R. C.).

References and notes

1 J. P. Rupert, W. T. Granquist and T. J. Pinnavaia, in *Chemistry of Clays and Clay Minerals*, ed. A. C. D. Newman, Longman Scientific & Technical, London, 1987, ch. 6.

2 H. Laudelout, in *Chemistry of Clays and Clay Minerals*, ed. A. C. D. Newman, Longman Scientific & Technical, London, 1987, ch. 4.

3 (*a*) D. P. Siantar, B. A. Feinberg and J. J. Fripiat, *Clays Clay Miner.*, 1994, **42**, 187–196; (*b*) P. B. Mitchell and K. Atkinson, *Miner. Eng.*, 1991, **4**, 1091–1113.

4 T. J. Pinnavaia and G. W. Beall, *Polymer-Clay Nanocomposites*, Wiley & Sons, Chichester, 2000.

5 R. E. Grim, *Clay Mineralogy*, McGraw-Hill, New York, 1968.

6 K. A. Carrado, *Appl. Clay Sci.*, 2000, **17**, 1–23.

7 K. A. Carrado and L. Xu, *Microporous Mesoporous Mater.*, 1999, **27**, 87–94.

8 (*a*) K. A. Carrado, L. Xu, C. L. Marshall, D. Wei, S. Seifert and C. A. Bloomquist, *Nanoporous Materials II*, ed. A. Sayari, M. Jaroniec, T. J. Pinnavaia, Elsevier, Amsterdam (*Stud. Surf. Sci. Catal.* vol. 129), 2000, 417–424; (*b*) K. A. Carrado, C. L. Marshall, J. R. Brenner and K. Song, *Microporous Mesoporous Mater.*, 1998, **20**, 17–26.

9 J. T. Kloprogge, *J. Porous Mater.*, 1998, **5**, 5–41.

10 K. Torii, Y. Onodera, T. Iwasaki, M. Shirai, M. Arai and Y. Nishiyama, *J. Porous Mater.*, 1997, **4**, 261–268.

11 J. T. Kloprogge, S. Komarneni and J. E. Amonette, *Clays Clay Miner.*, 1999, **47**, 529–555.

12 K. A. Carrado, L. Xu, D. M. Gregory, K. Song, S. Seifert and R. E. Botto, *Chem. Mater.*, 2000, **12**, 3052–3059.

13 (*a*) K. A. Carrado, P. Thiyagarajan and K. Song, *Clay Miner.*, 1997, **32**, 29–40; (*b*) K. A. Carrado, G. W. Zajac, K. Song and J. R. Brenner, *Langmuir*, 1997, **13**, 2895–2902.

14 (*a*) K. A. Carrado, J. E. Forman, R. E. Botto and R. E. Winans, *Chem. Mater.*, 1993, **5**, 472–478; (*b*) K. A. Carrado, *Ind. Eng. Chem. Res.*, 1992, **31**, 1654–1659.

15 K. A. Carrado, L. Xu, R. Csencsits and J. V. Muntean, *Chem. Mater.*, 2001, **13**, 3766–3773.

16 For a full description of the instrument see http://www.bessrc.aps.anl.

17 A. E. Bennett, C. M. Reinstra, M. Auger, K. V. Lakshmi and R. G. Griffin, *J. Chem. Phys.*, 1995, **103**, 6951.

18 (*a*) S. Komarneni, C. A. Fyfe, G. J. Kennedy and H. Strobl, *J. Am. Ceram. Soc.*, 1986, **69**, C45; (*b*) C. A. Weiss, S. P. Altaner and R. J. Kirkpatrick, *Am. Miner.*, 1987, **72**, 935; (*c*) R. A. Kinsey, R. J. Kirkpatrick, J. Hower, K. A. Smith and E. Oldfield, *Am. Miner.*, 1985, **70**, 537.

19 F. J. Berry, M. H. B. Hayes and S. L. Jones, *Inorg. Chim. Acta*, 1990, **178**, 203.

20 J. D. F. Ramsay, S. W. Swanton, A. Matsumoto and D. G. C. Goberdhan, in *The Colloid Chemistry of Silica*, ed. H. E. Bergna (*Adv. Chem. Ser.* 234), American Chemical Society, Washington, DC, 1994, p. 67.

21 D. W. Sindorf and G. E. Maciel, *J. Am. Chem. Soc.*, 1983, **105**, 3767.

22 G. Beaucage, *J. Appl. Crystallogr.*, 1995, **28**, 717–728.

23 K. C. Littrell, N. R. Khalili, M. Campbell, G. Sandi and P. Thiyagarajan, *Chem. Mater.*, 2002, **14**, 327–333.

24 K. S. W. Sing, D. H. Everett, R. A. W. Haul, L. Moscou, R. A. Pierotti, J. Rouquerol and T. Siemieniewska, *Pure Appl. Chem.*, 1985, **57**, 603–619.

25 D. W. Rutherford, C. T. Chiou and D. D. Eberl, *Clays Clay Miner.*, 1997, **45**, 534–543.

26 P. A. Webb and C. Orr, *Analytical Methods in Fine Particle Technology*, Micromeritics Instrument Corp., Norcross, GA, 1997, ch. 3.

27 T. J. Pinnavaia, V. Rainey, M. S. Tzou and J. W. White, *J. Mol. Catal.*, 1984, **27**, 213–224.

28 T. Neugebauer, *Ann. Phys. (Leipzig)*, 1943, **42**, 509.

29 G. Porod, *Acta Phys. Austriaca*, 1947, **2**, 258–260.

30 S. K. Sinha, T. Freltoft and J. K. Kjems, in *Kinetics of Aggregation and Gelation*, ed. F. Family and D. P. Landau, Amsterdam, Elsevier, 1984, pp. 87–90.

31 H. D. Bale and P. W. Schmidt, *Phys. Rev. Lett.*, 1984, **53**, 596–599.

32 G. Porod, *Kolloid Z.*, 1951, **124**, 93–94.

33 P. W. Schmidt, D. Anvir, D. Levy, A. Hohr, M. Steiner and A. Roll, *J. Chem. Phys.*, 1991, **94**, 1474–1479.

34 K. A. Carrado and S. M. Macha, unpublished results.